Multi-scale Cu-Cr composites using elemental powder blending in laser powder-bed fusion

Lucas Varoto, Pierre Lhuissier, Sophie Roure, Anthony Papillon, Mélissa Chosson, Camille Pauzon, Xavier Bataillon, Marc Fivel, Elodie Boller, Pierre Lapouge, et al.

Multi-Scale Cu-Cr Composites Using Elemental Powder Blending in Laser Powder-Bed Fusion

Lucas Varoto [1,2*], Pierre Lhuissier[2], Sophie Roure[1], Anthony Papillon[1], Mélissa Chosson[1], Camille Pauzon[2], Xavier Bataillon[2], Marc Fivel[2], Elodie Boller[3], Pierre Lapouge[4], Pierre Hébrard[4], Guilhem Martin[2]

[1] Schneider Electric Industries, F-38000 Grenoble, France
[2] Univ. Grenoble Alpes, CNRS, Grenoble INP, SIMaP, F-38000 Grenoble, France
[3]ESRF – The European Synchrotron, 71 avenue des Martyrs 38043 Grenoble, France
[4]Ecole Nationale Supérieure des Arts et Métiers, Laboratoire de Procédés et Ingénierie en Mécanique des Matériaux PIMM, UMR 8006 CNRS, 151, Boulevard de l'Hôpital, 75013, Paris, France
e-mail: lucas.varoto@grenoble-inp.fr

Abstract
Cu-Cr-based alloys are good candidates for thermo-electrical applications because of their excellent combination of mechanical, thermal, and electrical properties. However, tailoring their microstructure via traditional processes such as sintering and casting remains a challenging task. Herein, we introduce a strategy to fabricate multiscale Cu-25Cr composites. This is achieved through *in-situ* alloying from elemental powder blending in laser powder-bed fusion. The process is monitored layer-by-layer using synchrotron X-ray microtomography. We show that by changing the melt-pool size and its overlap, one can produce multiscale Cu-Cr composites with coarse (~50µm) and fine Cr-spheroids (<500 nm) while controlling their spatial distribution. Coarse Cr particles are preferentially located at the melt pool boundaries while fine spherical Cr particles are distributed in the melt pool interior. Spatial variations in mechanical properties are revealed using nanoindentation mapping. This strategy opens new opportunities to optimize multiscale metal matrix composite through the manipulation of the scanning strategy.

Keywords: Cu-Cr alloys; X-Ray Computed Tomography (XCT); Metal matrix composites; laser powder bed fusion

Cu-Cr-based alloys have been investigated because of their excellent combination of electrical, thermal, and mechanical properties [1-4]. Low alloyed Cu-Cr (with Cr<5%wt), often combined with Zr, Nb, or Mg addition, are known for their excellent strength-conductivity trade-off [1, 3-6]. In comparison with pure Cu, an increase of 200 MPa combined with a 20%IACS decrease can be achieved. The strength results from the superposition of precipitation and dispersion strengthening while the electrical and thermal conductivity remains relatively high due to a depleted solid solution, making them suitable for welding electrodes, cable connectors, and electrical-thermal conductors [1]. Highly alloyed Cu-Cr alloys (20<Cr<50%wt.) are used in severe thermo-electrical applications, such as medium voltage electrical contacts, for their composite properties: electrical conductivity of Cu and refractory properties of Cr [2, 7-10]. Due to the relatively low solubility of Cr in Cu (~0.7%wt. at 1070°C), these alloys can be considered metal matrix composites. In addition, it has been shown that the Cu-Cr system presents a large metastable miscibility gap (MG) and spinodal decomposition region (SD) under out-of-equilibrium solidification conditions [11-15]. This drastically changes the size and morphology of the Cr-phase. Despite the interest in Cu-Cr composites, the design and optimization of their microstructures have been constrained to the limits imposed by their conventional manufacturing processes (solid-state sintering and vacuum-casting).

Laser powder bed fusion (LPBF) has been extensively used to fabricate materials from pre-alloyed powders [16-18]. New trends and strategies have drawn the interest to expand the opportunities offered by additive manufacturing to produce new alloys [19-21] or compositionally graded materials [22-24] using elemental powder blends. This brings several important advancements to the processing of immiscible alloys and the design of composite-like microstructures. In addition, the development of novel scanning strategies to control the microstructures has pushed the limits even further in achieving site-specific microstructures [25-27]. Furthermore, the use of *in-situ* and *operando* techniques with

synchrotron radiation source to monitor the laser-matter interaction, such as X-ray radiography, acoustic emissions, or X-ray diffraction has raised our knowledge and understanding of the melt-pool dynamics, defects formation, and phase transformations [28-33]. Recently, synchrotron X-ray computed microtomography (SXCT) was proven to be efficient in monitoring in 3D the layer-by-layer LPBF process [34-36]. Monitoring layer-by-layer the sample and the powder bed can provide valuable information to better understand the process and to obtain a detailed 3D characterization of the powder bed and melt tracks during the build.

Herein, we introduce a strategy to fabricate multi-scale Cu-Cr metal matrix composites using LPBF. An elemental Cu+Cr powder blend was used for *in-situ* alloying. The process was monitored with layer-by-layer SXCT and the resulting microstructures are characterized using SEM and the local mechanical heterogeneities are revealed with nanoindentation mapping.

Pure Cu and Cr powders (characteristics are summarized in *Table 1*) were mixed in a Turbula® powder mixer in a 3:1 mass fraction (25%wt. Cr) for 30 minutes. The powder blend was then analyzed by laboratory XCT by filling a 1 mm-diameter glass tube with the powder mixture followed by XCT scans. The scans were acquired using an EasyTom XL-nano laboratory tomograph from RX Solutions. Reconstructions were made by filtered back projection. The experimental setup resulted in a voxel size of 1.80 µm. This allows the evaluation of the apparent density, i.e. packing density, as well as the chemical composition, i.e. local Cr density, estimated as follows: $Cr/(Cr + Cu)$ in the blend from short-range to long-range volumes (from 40 to 800 µm³). The average apparent density (XCT analysis) was compared to the apparent density measured using the Hall flowmeter considering the theoretical Cu-25Cr density as 8.40 g/cm³. A dedicated miniature LPBF machine for SXCT monitoring was used to print the Cu-Cr composites and monitor the layer-by-layer process. For more details and specifications regarding the LPBF replicator, see [34, 35]. These experiments were conducted at the BM18 beamline of the European Synchrotron Radiation Facility (ESRF). SXCT scans were acquired after layer deposition and after selective melting with 3000 projections over 180° resulting in an acquisition time of 2.5 minutes. A 10x6 mm² wide 135keV beam and an Iris detector (~5000×3000 pixels) coupled with a zoom optic and a 250µm thick LuAG scintillator were used to probe a large field of view while keeping a small voxel size of 2.08 µm. Reconstructions were also made by the filtered back projection method using Nabu.

*Table 1: Properties of the elemental powders (Cu and Cr) and the Cu-25Cr blend. *Hall's Cone apparent density was calculated considering the theoretical Cu-25Cr density as 8.40 g/cm³:*

	Cu	**Cr**	**Cu-25Cr**
D_V10 (µm)	46	42	
D_V50 (µm)	70	60	
D_V90 (µm)	107	80	
Sphericity$_V50$	> 0.90	> 0.90	
Apparent Density (XCT/ Halls Cone*)			55/52 %

Five samples made of five adjacent tracks were printed on an 8 mm-diameter build plate. A simple bi-directional scanning strategy with no rotation from one layer to another was employed. The hatch spacing was set to 120 µm and the layer thickness to 50 µm. Power was kept constant at 400 W and speed varied between 200 and 600 mm/s depending of the sample. This simple printing strategy allows the direct cross-evaluation of Cu-Cr melting conditions and the effect of variations in scanning speed on the microstructure.

The reconstructed images were analyzed in planes parallel and perpendicular to the building direction (BD). With such a resolution, only the coarse Cr-particles (> 15 µm) can be accurately identified and followed. A Zeiss Gemini 500 FEG Scanning electron microscope (SEM) was used to investigate the microstructure at a finer scale. Nano-indentation mapping using an Anton-Paar NHT3 tester was used at a constant strain rate of 0.05 s^{-1}, maximum load of 10 mN, and 10 s loading pause. A 31×31 indentation grid was made with a 15 µm spacing in the 200, 400, and 600 mm/s samples to correlate the local changes in microstructure to variations in mechanical properties.

Figure 1a shows a 2D cross-section extracted from the XCT images of the powder blend. The Cu and Cr powder particles can be distinguished due to the difference in attenuation coefficient. Cu and Cr particles have relatively high sphericity and Cu powder presents some internal pores. Throughout the different short-range and long-range volumes analyzed in the powder blend, a resulting average apparent density of 55% and a Cr powder particle density approaching 27% were determined (**Figure 1b**). This is consistent with the apparent density measured using the Hall Flowmeter and the initial alloy composition (25%wt Cr). However, as the powder blend volume of interest decreases, the deviation from the average increases significantly for both properties, as indicated by the error bars in **Figure 1b**. Thus, at the melt pool scale (of the order of 100-200 µm³), significant local heterogeneities in the powder packing and Cr powder particle density are expected in the powder bed. A cross-section extracted from the SXCT images of the powder bed during the build (**Figure 1c**) highlights the spatial heterogeneities when using small probe volumes.

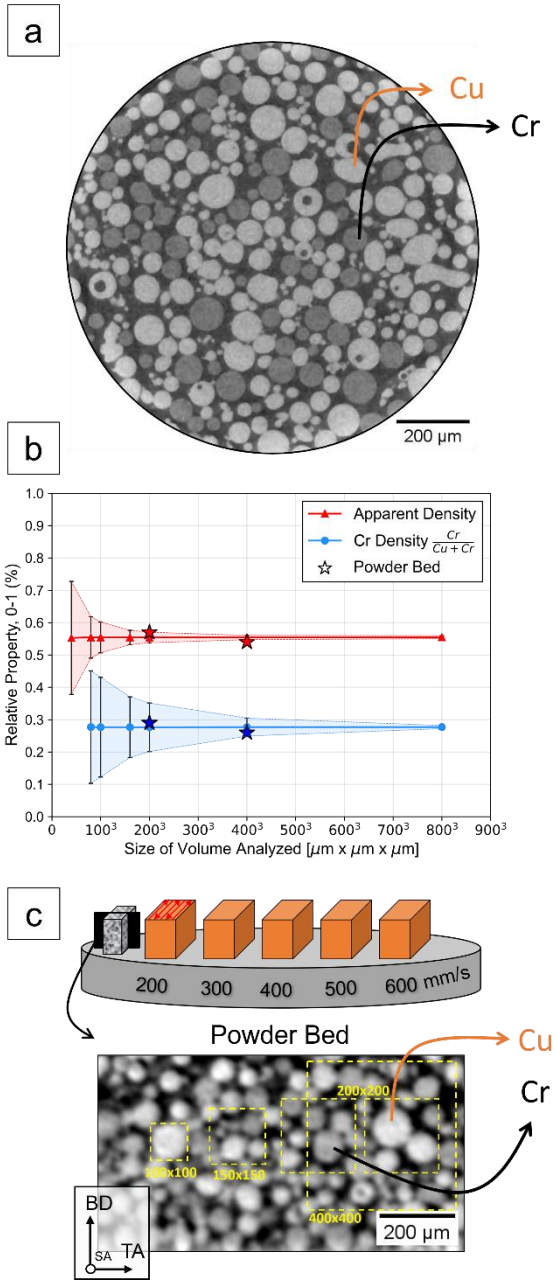

Figure 1: a) 2D cross-section extracted from the XCT scan of the Cu-25Cr powder (voxel size = 1.80 µm). b) Average Relative Property (from 0 to 1): apparent packing density and Cr particle density as a function of the volume size analyzed from XCT images. The error bars are associated with the standard deviation from the

average. The star symbols correspond to the results measured directly in the powder bed during printing. c) Schematic showing the samples on the building substrate along with a 2D cross-section of the powder bed in the LPBF replicator extracted from SXCT scans showing the packing and distribution of Cu and Cr particles (voxel size = 2.08 µm). Boxes of different areas from 100×100 to 400×400 µm² are drawn to illustrate the local heterogeneities shown in b) .

Figure 2a shows SXCT 2D-transverse cross-sections taken at the half height of the 200, 400, and 600 mm/s samples after the completion of about 20 layers. The alignment of darker grey structures parallel to the scanning direction SA as well as their size and density from 200 to 600 mm/s can be distinguished. The normalized average greyscale profiles across the sample along the TA shown in **Figure 2b** reveal the presence of such structures. The wave-like profiles reflect the change in Cr-composition, where the valleys indicate Cr-rich zones (Cr-walls) and the peaks are associated with Cu-rich zones. From 200 to 600 mm/s, the amplitude of such wave-like profiles becomes more pronounced showing the presence of larger and denser Cr-wall structures. Interestingly, the Cr-rich zones are spaced by a distance equal to the hatch spacing (120µm). The porosity fraction profile inside each sample is also plotted. The volume fraction of pores increases from 200 to 600 mm/s and seems preferentially located in the Cu-rich zones (in-between Cr-walls). The preferential location of the pores (at the melt pool center) and the processing conditions employed suggest that those defects are keyhole pores. This will be confirmed later by the observation of the melt pool morphology (**Figure 4**). The decrease in speed from 600 to 200 mm/s results in the increase of the melt pool overlap, thus healing the porosity resulting from the keyhole mode and increasing sample density as shown in [35]. The 3D reconstruction of three samples and selected zoom inside the two extreme conditions are shown in **Figure 2c-d**. The walls consisting of coarse Cr particles aligned along the laser direction and rising along BD can be observed (**Figure 2c-d**). As the speed increases, the partially molten Cr particles get larger and more numerous, producing a different scale for the formation of such Cr-walls.

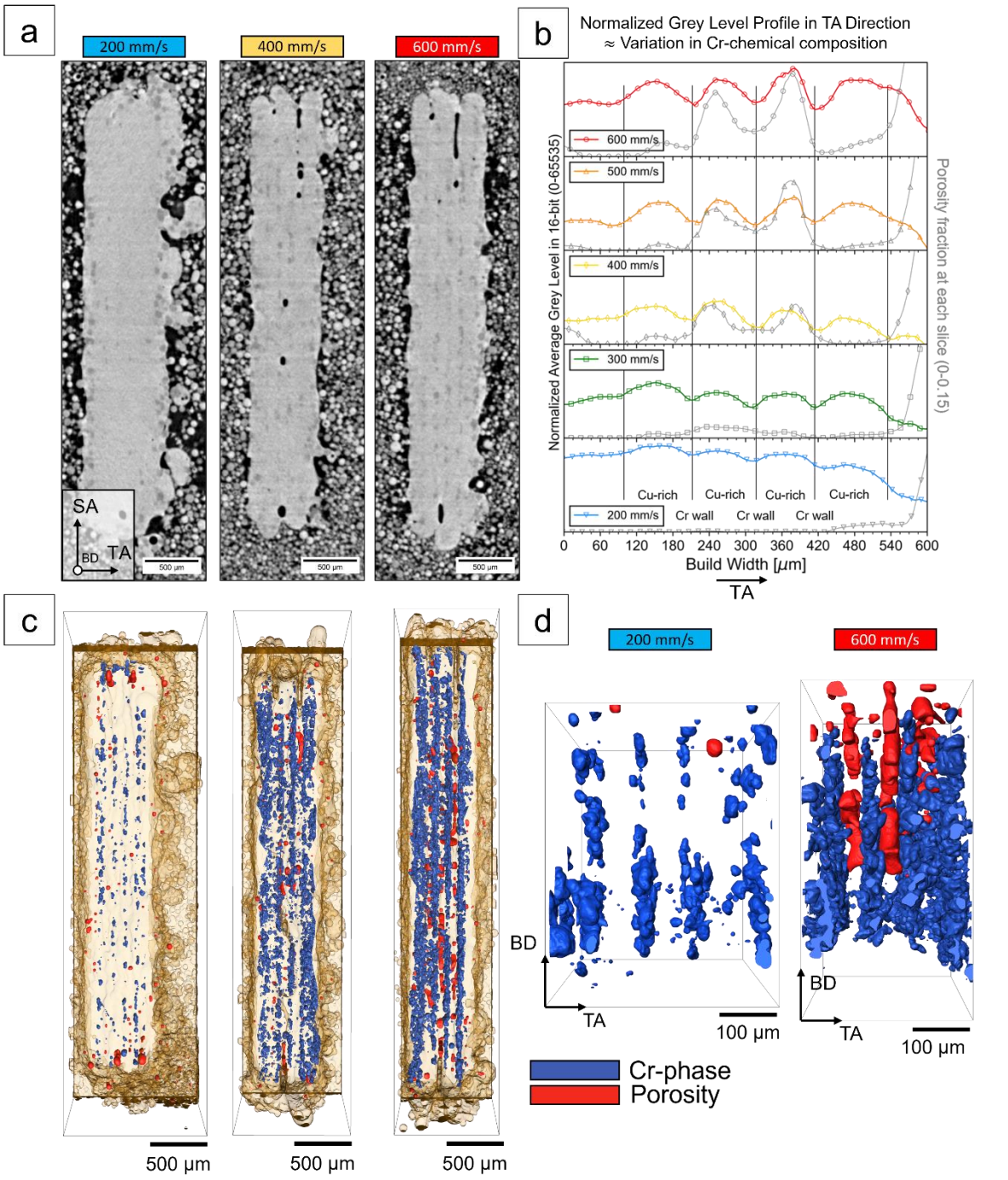

Figure 2: a) SXCT 2D-transverse cross-sections (taken at half height) showing the total length of the Cu-25Cr composites for the 200, 400, and 600 mm/s laser speed. The Cr-walls are aligned along the laser direction as shown by the darker grey level associated with coarse Cr particles; b) Normalized grey level profile (which reflects the local Cr particle density along the TA direction) and pore volume fraction in the TA direction (averaged across the whole thickness of the sample); c-d) 3D rendering of the 200, 400, and 600 mm/s Cu-25Cr samples showing in blue the rise and alignment of the Cr-walls and the presence of pores in red in-between

The mechanism leading to the formation of such Cr-walls made of coarse Cr-particles and aligned with BD is illustrated in **Figure 3a-c**. The layer-by-layer SXCT monitoring highlights the formation and evolution (from layers #8 to #16) of these Cr-walls (**Figure 3a**). The Cr-powder tracking and its local powder bed heterogeneity before melting strongly influence the subsequent layer. Depending on the laser speed, partially melted Cr or unmolten Cr particles can be identified inside the samples, see the white circles in **Figure 3a**. The thermal conditions established for a given speed result in partial Cr-

melting due to the difference in melting temperature between Cu (1084 °C) and Cr (1907 °C). The convection flows (predominantly Marangoni convection) tend to carry the partially molten Cr particles to the sides of the melt pool, as captured by the *operando* monitoring in **Figure 3b** [29, 31]. Therefore, by varying the speed from 200 to 600 mm/s, one can adjust the overlap between adjacent tracks. In addition, the energy density distribution delivered by the focused laser also changes throughout the melt pool. Higher energy density, thus temperature, is expected at the center of the melt pool in comparison with the melt pool sides due to the Gaussian distribution of the laser intensity. Therefore, large partially melted Cr-particles are preferentially located at the melt pool sides and separated by the hatching distance (**Figures 3b** and **c**). As there is no rotation of the scanning pattern, this local accumulation of large Cr-particles will rise with the addition of new layers, forming Cr-walls parallel to the laser direction. The change in melt pool size due to a change in speed defines the degree of remelting of such partially melted coarse Cr-particles while melting the adjacent track and subsequent layer (**Figure 3c**). Lower speeds lead to larger melt pools and, consequently larger overlaps between adjacent tracks. Thus, one can expect smaller and fewer Cr-particles left from melting and remelting due to overlapping at low speeds. Alternatively, higher speeds lead to smaller melt pools and, consequently smaller overlaps between adjacent tracks resulting in a larger, and greater number of coarse Cr-particles left.

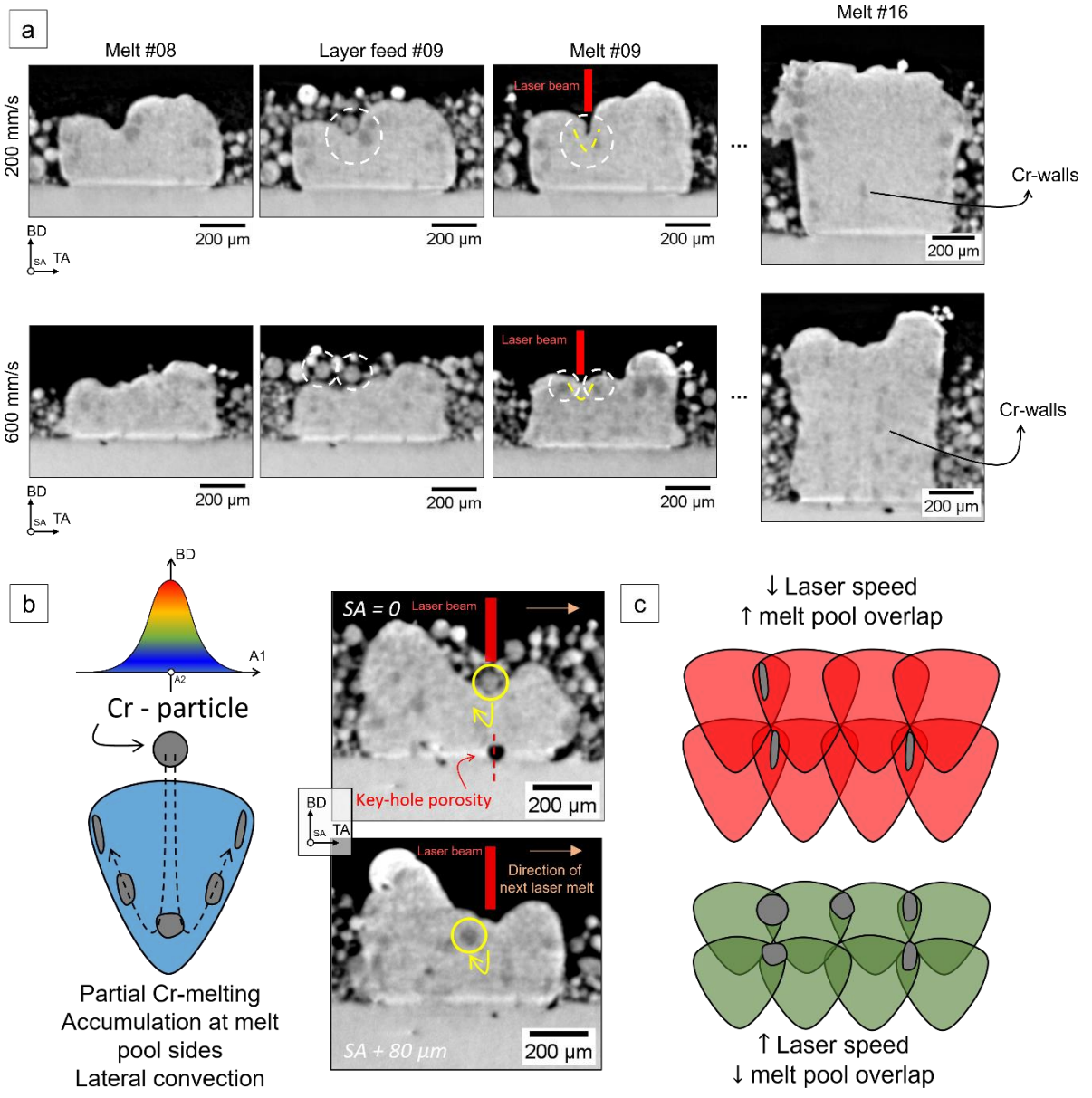

Figure 3: a) Series of SXCT images collecting during the build and showing the formation of Cr-walls in samples processed using varying speeds: 200, and 600 mm/s respectively; b) Schematic representation of the partial melting

of Cr-particles inside a melt pool considering a Gaussian energy density profile for the laser heat source with an experimental example captured by SXCT layer-by-layer monitoring; c) The different overlaps between larger and smaller melt pools due to lower and higher laser speeds, respectively.

Figures 4a-d, **e-h**, and **i-l** show the SEM-BSE images of the 200, 400 and 600 mm/s samples, respectively showing their multiscale microstructure. The high-magnification images revealing the microstructures in more detail were taken at an equivalent position inside the melt pool with respect to the bottom of the melt pool. The effect of the laser speed on the formation of the Cr-walls is illustrated in **Figures 4a**, **e**, **and i**. The greater melt pool overlaps (low speed) result in a more homogeneous Cr-melting with the formation of finer Cr-walls, the latter consisting of a lower density of Cr coarse particles (**Figure 4a-b**). As the speed increases, melt pool overlap decreases leading to partial melting of Cr coarse particles and the formation of thicker and denser Cr-walls, see **Figure 4e-f** and **i-k** respectively. The black dotted lines in **Figure 4e** and **j** highlight some melt-pool boundaries confirming that their morphology is typical of a keyhole regime (depth >> width). The accumulation of Cr coarse particles along the side of melt pools forming Cr-walls is clear, especially at 200 and 400 mm/s. In the 600 mm/s sample, the process parameters and thermal conditions are such that a few partially melted Cr particles can be observed out of the melt pool sides, producing a more random distribution of the Cr coarse particles in the microstructure. Inside the melt pools, fine Cr-spheroids can be observed regardless of the processing conditions. These microstructures result from the liquid-liquid phase separation followed by rapid solidification in agreement with what was reported in other Cu-based immiscible alloys (Cu-Co and Cu-Fe systems [37-41]). Due to the out-of-equilibrium solidification conditions inherent to LPBF, the Cu-25Cr alloy undergoes high undercooling conditions entering the metastable miscibility gap. Under rapid solidification conditions, the homogenous liquid phase of immiscible alloys presenting a large miscibility gap separates into two liquid phases, here a Cr-rich and a Cu-rich liquid phase. The minority phase takes a spherical morphology to minimize the surface energy. In the 200 mm/s case, such Cr-spheroids in the melt pools appear to be relatively larger and more homogeneous in size and distribution (**Figures 4d-c**). For 400 and 600 mm/s samples, finer Cr-spheroids present some local heterogeneity in size and distribution, especially from the inside of the melt pool to its sides, see **Figures 4f-g** and **4j-k**. These local heterogeneities result from less efficient remelting conditions that do not completely erase the local chemical heterogeneities present initially in the powder bed. Therefore, relatively larger and more homogeneous Cr-spheroids are formed due to better remelting and slower solidification rate in the 200 mm/s sample. More heterogeneous distribution but smaller Cr-spheroids are found in both 400 and 600 mm/s samples due to higher solidification rate and lower remelting.

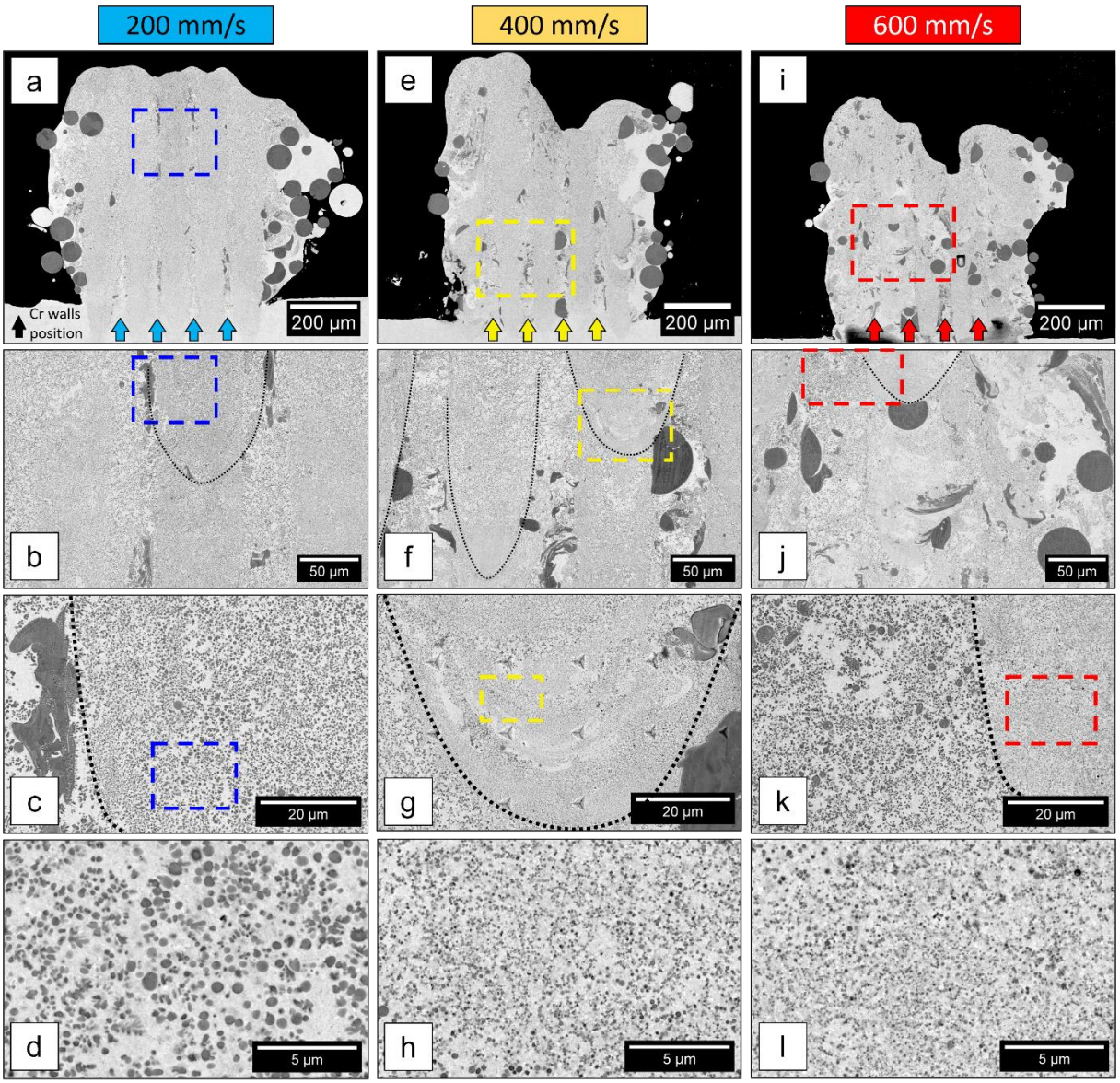

Figure 2: SEM-BSE images of the multiscale microstructure, from an overall view showing the entire sample's cross-section down to the nanoscale microstructure in the melt pool interior: a-d) sample printed at 200 mm/s, e-h) sample printed at 400 mm/s, and i-l) sample printed at 600 mm/s. Arrows in a, e, and i help to locate the position of the Cr-walls. Dotted lines indicate the position of a few melt pool boundaries.

The nanoindentation maps of the 200, 400, and 600 mm/s samples along with Cr-size correlation maps are shown in **Figures 5a-f**. The hardness map (HIT in MPa) and a selected region are overlayed with the corresponding microstructure for each sample. Improper dwells from the indentation testing are not considered and displayed in black in the hardness maps. The proposed strategy to print Cu-Cr samples based on the melt pool size and overlap generates a gradient in hardness between Cr-walls along the TA direction. Higher hardness values can be found at the center of the melt pools, whereas lower values are found at the melt pool sides in regions not decorated with coarse Cr particles. In addition, the partially melted Cr particles forming the walls parallel to the BD act as a hard phase with significantly higher hardness. In the hardness maps of the 200 and 400 mm/s samples a layered pattern can be observed (**Figures 5a-b** and **5d-e**). In the 600 mm/s sample, the heterogeneous microstructure produced by the smaller melt pools and its overlap masks such gradient in hardness by the presence of partially melted Cr-particles (**Figures 5g-f**). Such hardness gradient corresponds well with the local changes in microstructure, as illustrated by the Cr-size correlation map in **Figures 5c**, **f**, and **l**. The Cr-phase size increases and the density of fine Cr-spheroids decreases from the middle of the melt pool to its sides (**Figure 4**). Due to more homogeneous melting at the melt pool center, Cr-powder particle melts more

efficiently forming the fine and dense region of Cr-spheroids during rapid solidification.

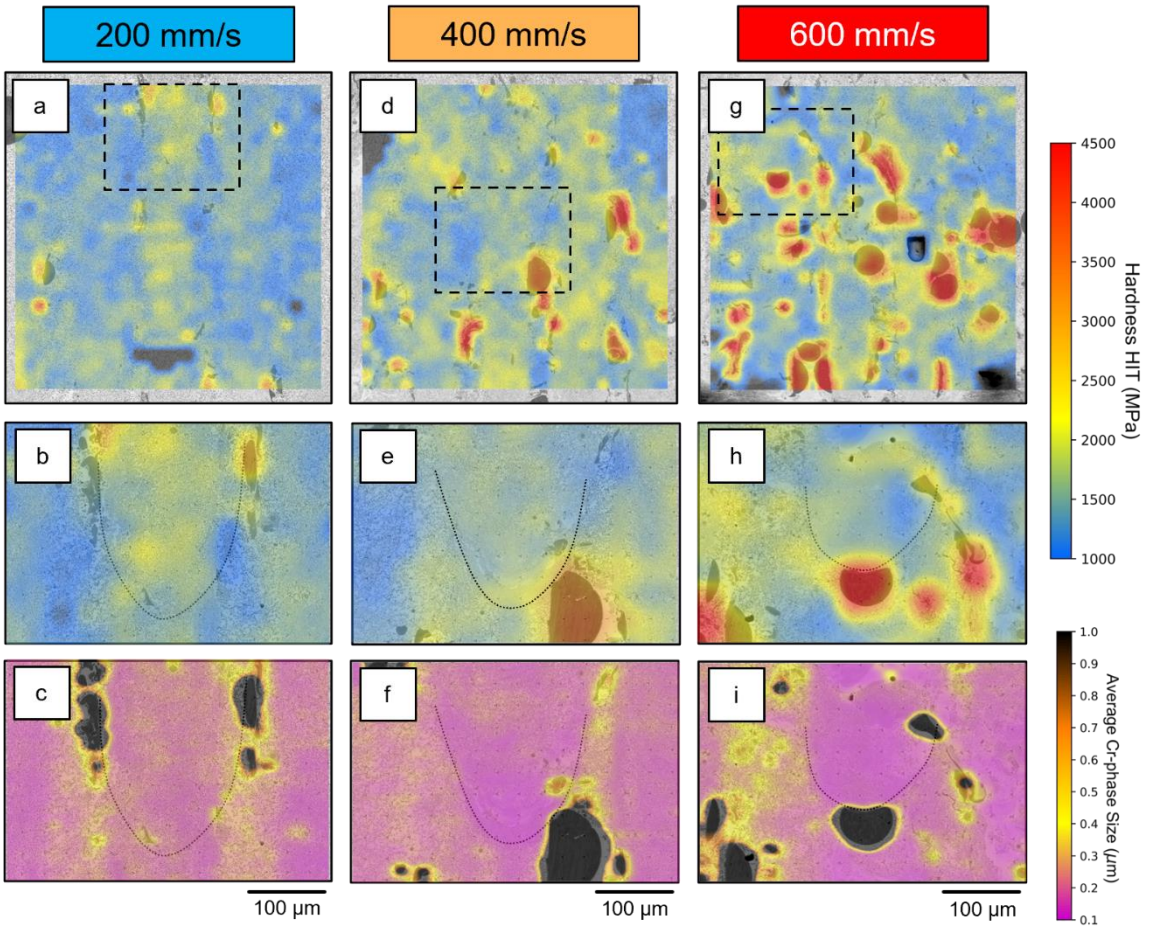

Figure 3: SEM/BSE image of the different samples superimposed with the corresponding nanohardness map for different speeds: a) 200 mm/s, d) 400 mm/s, and g) 600 mm/s. A selected region of the microstructure, same as in Figures 4d, f, and j with the corresponding hardness and Cr-size correlation map overlayed for b-c) 200 mm/s, e-f) 400 mm/s, and h-i) 600 mm/s. respectively.

Cu-Cr multiscale composites were successfully fabricated by *in-situ* alloying using an elemental Cu and Cr powder mixture in LPBF. The fabrication was monitored layer-by-layer using SXCT to shed light on some mechanisms involved in microstructure formation. We show how the microstructure of such Cu-Cr composites can be tailored by adjusting the processing conditions. The proposed strategy opens new opportunities to tailor and control the microstructure of immiscible alloys by manipulating the scanning strategy (hatch spacing, rotation of the scanning pattern, layer thickness). Such strategy can be expanded to other immiscible alloy systems in the future.

Acknowledgments

The authors are grateful to Schneider Electric Industries and the Association Nationale de la Recherche Technologique (ANRT) for the financial support of this work in the framework of the Ph.D. of Lucas Varoto (CIFRE 2021/1619). This work has benefited from the characterization equipment of the Grenoble INP CMTC platform supported by the Centre of Excellence of Multifunctional Architectured Materials "CEMAM" n◦ANR-10-LABX-44-01 funded by the Investments for the Future program. The European Synchrotron Radiation Facility (ESRF) is gratefully acknowledged for offering beamtime at BM18 associated with the proposal MA4928. The authors wish to thank Patrice Peyre and Frédéric Coste, from ENSAM Paris for their help and assistance with the manipulation of the laser device.

References

[1] J. R. Davis, Copper and Copper Alloys, ASM Specialty Handbook, ASM International, 2001, ISBN: 0-87170-726-8

[2] P. G. Slade, The Vacuum Interrupter: Theory, Design, and Application, Boca Raton: CR Press Taylor & Francis Group, 2008, ISBN 978-0-8493-9091-3

[3] X. Tang, X. Chen, F. Sun, P. Liu, H. Zhou, S. Fu, The current state of CuCrZr and CuCrNb alloys manufactured by additive manufacturing: A review, Materials & Design 224 (2022), 111419, https://doi.org/10.1016/j.matdes.2022.111419

[4] H. Tang, Z. Ma, C. Lei et al. High strength and high conductivity Cu alloys: A review. Sci. China Technol. Sci. 63 (2020), 2505–2517, https://doi.org/10.1007/s11431-020-1633-8

[5] S. Uchida, T. Kimura, T. Nakamoto, T. Ozaki, T. Miki, M. Takemura, Y. Oka, R. Tsubota, Microstructures and electrical and mechanical properties of Cu-Cr alloys fabricated by selective laser melting, Materials & Design, 175 (2019) 107815, https://doi.org/10.1016/j.matdes.2019.107815

[6] Y. Li, B. Yang, P. Zhang, Y. Nie, X. Yuan, Q. Lei, Y. Li, Cu-Cr-Mg alloy with both high strength and high electrical conductivity manufactured by powder metallurgy process, Materials Today Communications 27 (2021), 102266, https://doi.org/10.1016/j.mtcomm.2021.102266

[7] A. Papillon, et al., Sintering mechanisms of Cu-Cr metallic composites, Int J Refract Met Hard Mater, 65 (2017), 9-13 http://dx.doi.org/10.1016/j.ijrmhm.2016.11.010

[8] C. Y. Zhang, Y. P. Wang, Z. M. Yang Z M, Y. Guo, B. J. Ding, Microstructure and properties of vacuum induction melted CuCr25 alloys, J. Alloys Compd. 366 (2004) 289–92, https://doi.org/10.1016/j.jallcom.2003.07.001

[9] J. Han, Z. Dou, T. Zhang, W. An, Review of the recent Chinese research on the electrical properties of CuCr contacts for vacuum interrupters, Journal of Materials Research and Technology 25 (2023), 1585-1598, https://doi.org/10.1016/j.jmrt.2023.06.060

[10] W. Huang, H. Yu, L. Wang, X. Wu, C. Ouyang, Y. Zhang, J. He, State of the art and prospects in sliver- and copper-matrix composite electrical contact materials, Materials Today Communications 37 (2023), 107256, https://doi.org/10.1016/j.mtcomm.2023.107256

[11]] X. Wei, J. Wang, Z. Yang, Z. Sun, D. Yu, X. Song, B. Ding, S. Yang, Liquid phase separation of Cu–Cr alloys during the vacuum breakdown, , J. Alloys Compd., 509 (2011), 7116-20, https://doi.org/10.1016/j.jallcom.2011.04.017

[12] S. Momeni, Ralf Guschlbauer, F. Osmanlic, C. Körner, Selective electron beam melting of a copper-chrome powder mixture, Materials Letters, 223 (2018), 250-52, https://doi.org/10.1016/j.matlet.2018.03.194

[13] Z.M. Zhou, J. Gao, F. Li et al. On the metastable miscibility gap in liquid Cu–Cr alloys. J Mater Sci 44 (2009), 3793–3799, https://doi.org/10.1007/s10853-009-3511-y

[14] Z.M. Zhou, J. Gao, F. Li et al. et al. Experimental determination and thermodynamic modeling of phase equilibria in the Cu–Cr system. J Mater Sci 46 (2011), 7039–7045, https://doi.org/10.1007/s10853-011-5672-8

[15] L. Zhang, G. Yu, X. He, S. Li, W. Ning, X. Wang, Journal of Alloys and Compounds 772 (2019), 209-217, https://doi.org/10.1016/j.jallcom.2018.08.012

[16] W. J. Sames, F. A. List, S. Pannala, R. R. Dehoff & S. S. Babu, The metallurgy and processing science of metal additive manufacturing, International Materials Reviews, 61 (2016), 315-360, https://doi-org/10.1080/09506608.2015.1116649

[17] MS. Pham, B. Dovgyy, P.A. Hooper et al. The role of side-branching in microstructure development in laser powder-bed fusion. Nat Commun, 749 (2020). https://doi.org/10.1038/s41467-020-14453-3

[18] M. Buttard, G. Martin, X. Bataillon, G. Renou, P. Lhuissier, J. Villanova, B. Chehab, P. Jarry, J-J. Blandin, P. Donnadieu, Towards an alloy design strategy by tuning liquid local ordering: What solidification of an Al-alloy designed for laser powder bed fusion teaches us, Additive Manufacturing 61 (2023), 103313, https://doi.org/10.1016/j.addma.2022.103313

[19] C. Pauzon, M. Buttard, A. Després, B. Chehab, J-J. Blandin, G. Martin, A novel laser powder bed fusion Al-Fe-Zr alloy for superior strength-conductivity trade-off, Scripta Materialia, 219 (2022), 114878, https://doi.org/10.1016/j.scriptamat.2022.114878

[20] Y. Liu, J. Zhang, Q. Tan, Y. Yin, S. Liu, M. Li, M. Li, Q. Liu, Y. Zhou, T. Wu, F, Wang, M-X. Zhang, Additive manufacturing of high strength copper alloy with heterogeneous grain structure through laser powder bed fusion, Acta Materialia 220 (2021), 117311, https://doi.org/10.1016/j.actamat.2021.117311

[21] Y. T. Tang, C. Panwisawas, J. N. Ghoussoub, Y. Gong, J.W.G. Clark, A.A.N. Németh, D. G. McCartney, R. C. Reed, Alloys-by-design: Application to new superalloys for additive manufacturing, Acta Materialia, 202 (2021), 417-436, https://doi.org/10.1016/j.actamat.2020.09.023

[22] S. Wei, Y. Zhao, S-H. Li, S. Chen, K. B. Lau, V. Soh, J. J. Lee, B. Zhang, C. Cheh Tan, P. Wang, U. Ramamurty, Laser powder bed fusion of a Cu-Ni-Al alloy using the compositional grading approach, Scripta Materialia 231 (2023), 115441, https://doi.org/10.1016/j.scriptamat.2023.115441

[23] D.C. Hofmann, J. Kolodziejska, S. Roberts et al. Compositionally graded metals: A new frontier of additive manufacturing. Journal of Materials Research 29 (2014), 1899–1910, https://doi.org/10.1557/jmr.2014.208

[24] I. Ferretto, A. Sharma, D. Kim, N.M. Della Ventura, X. Maeder, J. Michler, E. Hosseini, W.J. Lee, C. Leinenbach, Fabrication of FeMnSi-based shape memory alloy components with graded-microstructures by laser powder bed fusion, Additive Manufacturing, 78 (2023), 103835, https://doi.org/10.1016/j.addma.2023.103835

[25] H. Li, S. Thomas, C. Hutchinson, Delivering microstructural complexity to additively manufactured metals through controlled mesoscale chemical heterogeneity, Acta Materialia 226 (2022), 117637, https://doi.org/10.1016/j.actamat.2022.117637

[26] R. R. Dehoff, M. M. Kirka, W. J. Sames, H. Bilheux, A. S. Tremsin, L. E. Lowe & S. S. Babu, Site specific control of crystallographic grain orientation through electron beam additive manufacturing, Materials Science and Technology, 31 (2015), 931-938, https://doi-org/10.1179/1743284714Y.0000000734

[27] S. Gao, Z. Li, S. Van Petegem *et al.* Additive manufacturing of alloys with programmable microstructure and

properties. *Nat Commun* 14 (2023), 6752, https://doi.org/10.1038/s41467-023-42326-y
[28] C. Zhao, K. Fezzaa, R. W. Cunningham et al. Real-time monitoring of laser powder bed fusion process using high-speed X-ray imaging and diffraction, Sci Rep, 7 (2017), 3602, https://doi.org/10.1038/s41598-017-03761-2
[29] C.L.A. Leung, S. Marussi, R.C. Atwood et al. In situ X-ray imaging of defect and molten pool dynamics in laser additive manufacturing. Nat Commun 9 (2018), 1355, https://doi.org/10.1038/s41467-018-03734-7
[30] R. Drissi-Daoudi, G. Masinelli, C. Formanoir, K. Wasmer, J. Jhabvala, R. E. Logé, Acoustic emission for the prediction of processing regimes in Laser Powder Bed Fusion, and the generation of processing maps, Additive Manufacturing, 67 (2023), 103484, https://doi.org/10.1016/j.addma.2023.103484
[31] Q. Guo, C. Zhao, M. Qu, L. Xiong, S. M. H. Hojjatzadeh, L. I. Escano, N. D. Parab, K. Fezzaa, T. Sun, L. Chen, In-situ full-field mapping of melt flow dynamics in laser metal additive manufacturing, Additive Manufacturing, 31 (2020), 100939, https://doi.org/10.1016/j.addma.2019.100939
[32] Y. Huang, T.G. Fleming, S.J. Clark et al. Keyhole fluctuation and pore formation mechanisms during laser powder bed fusion additive manufacturing. Nat Commun 13 (2022), 1170, https://doi.org/10.1038/s41467-022-28694-x
[33] C. Kenel, D. Grolimund, X. Li et al. In situ investigation of phase transformations in Ti-6Al-4V under additive manufacturing conditions combining laser melting and high-speed micro-X-ray diffraction. Sci Rep 7 (2017), 16358, https://doi.org/10.1038/s41598-017-16760-0
[34] P. Lhuissier, X. Bataillon, C. Maestre, J. Sijobert, E. Cabrol, P. Bertrand, E. Boller, A. Rack, J-J. Blandin, L. Salvo, G. Martin, In situ 3D X-ray microtomography of laser-based powder-bed fusion (L-PBF)—A feasibility study, Additive Manufacturing 34 (2020), 101271, https://doi.org/10.1016/j.addma.2020.101271
[35] P. Lhuissier, L. Hébrard, X. Bataillon, P. Lapouge, F. Coste, P. Peyre, E. Boller, J-J. Blandin, L. Salvo, G. Martin; Miniature laser powder bed fusion system for in situ synchrotron x-ray micro-computed tomography experiments at the European Synchrotron Radiation Facility. Rev. Sci. Instrum. 93 (2022), 083701. https://doi.org/10.1063/5.0090623
[36] M. G. Makowska, F. Verga, S. Pfeiffer *et al.* Operando tomographic microscopy during laser-based powder bed fusion of alumina. *Commun Mater* **4 (2023)**, https://doi.org/10.1038/s43246-023-00401-3
[37] L. Ratke, S. Diefenbach, Liquid immiscible alloys, Materials Science and Engineering: R: Reports 15 (1995), 263-347, https://doi.org/10.1016/0927-796X(95)00180-8
[38] I. Yamauchi, N. Ueno, M, Shimaoka *et al.* Undercooling in Co–Cu alloys and its effect on solidification structure. *Journal of Materials Science* 33 (1998), 371–378, https://doi-org/10.1023/A:1004319829612
[39] C. Wei, J. Wang, Y. He, Y. Yan, J. Gao, J. Li, E. Beaugnon, Liquid-liquid phase separation in immiscible Cu-Co alloy, Materials Letters, 268 (2020), 127585, https://doi.org/10.1016/j.matlet.2020.127585
[40] W. Wang, Y. Wu, L. Li *et al.* Liquid-liquid phase separation of freely falling undercooled ternary Fe-Cu-Sn alloy. *Sci Rep* 5 (2015), 16335, https://doi.org/10.1038/srep16335
[41] J. Zhang, X. Cui, Y. Wang, Liquid phase separation in immiscible Cu–Fe alloys, International Journal of Cast Metals Research, 31 (2018) , 87-92, https://doi-org/10.1080/13640461.2017.1367527

Graphical Abstract